



Oxidation of 1,2-dichloroethane over nanocube-shaped Co_3O_4 catalysts

J. González-Prior, R. López-Fonseca, J.I. Gutiérrez-Ortiz, B. de Rivas*

Chemical Technologies for Environmental Sustainability Group, Department of Chemical Engineering, Faculty of Science and Technology, University of The Basque Country (UPV/EHU), PO Box 644, E-48080 Bilbao, Spain

ARTICLE INFO

Article history:

Received 18 March 2016
Received in revised form 3 June 2016
Accepted 18 June 2016
Available online 23 June 2016

Keywords:

Catalytic oxidation
1,2-Dichloroethane
Nanostructured cobalt oxide
Oxygen mobility
Nanocubes

ABSTRACT

The synthesis of a series of bulk cobalt oxides with different nanostructure (nanocube, nanosheets and nanorods) has been attempted and their performance has been evaluated for the oxidation of 1,2-dichloroethane, one of the most common chlorinated pollutants found in waste streams. Structural, morphological and physicochemical properties have been analysed by X-ray diffraction, Raman spectroscopy, BET measurements, SEM, HRTEM, XPS and temperature-programmed reduction with hydrogen. It has been found that the morphology plays a key role in determining the catalytic behaviour, being the nanocube-shaped oxides the most active catalysts. This catalyst has led the total oxidation of DCE towards CO_2 , HCl and Cl_2 at relatively low temperatures (400°C) without by-products formation. Both activity and selectivity of Co_3O_4 with this morphology are controlled by a high surface area, a low crystallite size, a highly defective structure and a good oxygen mobility within the lattice.

© 2016 Elsevier B.V. All rights reserved.

1. Introduction

Industrial emissions containing chlorinated VOCs such as dichloromethane, chloroform, carbon tetrachloride, 1,2-dichloroethane and trichloroethylene require special attention due to high toxicity and stability of these gaseous pollutants. Additionally, these compounds are linked with the formation of low-level ozone and photochemical smog, stratospheric ozone depletion, and are considered greenhouse gases [1]. Catalytic combustion is proposed as an effective technique for the total elimination of chlorinated VOCs from flue gases, owing to its low operating temperatures and high activity and selectivity with a capacity to oxidise completely the pollutants without the production of harmful by-products [2].

Currently, the most active catalysts are those based on platinum and palladium, which are dispersed on a high surface area support. Noble metals are powerful oxidation catalysts but they are very sensitive to poisoning by chlorine and have high costs and limited availability [3]. An alternative to noble-metal based catalysts are cheaper metal oxide catalysts. Particularly, Co_3O_4 with a spinel structure has been shown to be one of the most efficient in the total oxidation of VOCs due to its high content of surface oxy-

gen species and/or the good mobility of oxygen species through the lattice [4,5]. Probably the main drawback is the relatively low thermal stability which frequently results in a substantial decrease in surface area and a marked sintering [6]. Bulk metal oxides can be obtained by various methods, including thermal decomposition, sol-gel processes, microemulsion methods, pyrolysis, precipitation, reduction-oxidation routes, hydrothermal/solvothermal synthesis or template procedures [4,6–9]. Considerable attention has been recently paid to optimising the catalytic properties of the spinel by tuning its nanomorphology [10]. In short, Co_3O_4 nanostructures with well-defined sizes, shapes, and crystallinity are usually prepared following a two-step process. Initially, the precursors with different shapes and novel structures are mainly synthesised by solution-based approaches, and subsequently are transformed to Co_3O_4 by thermal decomposition at elevated temperatures. In this sense it is quite important to control the morphology from the precursors to the final spinel nanostructures while optimising the population of highly active oxygen species. In addition, the achieved morphologies must be thermally stable in the typical temperature window for oxidation of VOC (300 – 550°C). The desired bulk metal oxide shapes are typically rods, crystals which grow in one direction preferentially; sheets, which grow in two directions; and three dimensional cubes. Some studies on the viability of these nanoshaped catalysts for oxidation of CO, non-chlorinated VOCs and methane can be found in the literature [11–14] but no reports on their performance for chlorinated VOC abatement are available.

* Corresponding author.

E-mail address: beatriz.derivas@ehu.eus (B. de Rivas).

In the present work a variety of Co_3O_4 samples with these predefined morphologies have been prepared, using an organic soft template followed by a hydrothermal treatment. These materials have been tested as catalysts in the total oxidation of 1,2-dichloroethane ($\text{C}_2\text{H}_4\text{Cl}_2$, DCE), which is chosen as a model of chlorinated VOC owing to its widespread presence in the flue gases of polyvinyl chloride plants, in a fixed-bed flow reactor. In order to establish useful relationships between structural, morphological and physicochemical properties of the spinels and their catalytic behaviour the prepared bulk oxides have been thoroughly characterised by X-ray diffraction, Raman spectroscopy, BET measurements, scanning electron microscopy, X-ray photoelectron spectroscopy and temperature-programmed reduction with hydrogen. This study has been further supported by kinetic modelling and evaluation of catalytic behaviour with time on stream.

2. Experimental

2.1. Catalysts preparation

A number of Co_3O_4 samples have been prepared following several routes devoted to synthesis of spinels with a controlled morphology (1D, 2D and 3D structures). Particularly two different methodologies were examined for each selected morphology (rods, sheets and cubes).

2.2.1. Samples with rod-like morphology (R samples – 1D shaped catalysts)

The R1 sample has been prepared mixing cobalt (II) chloride (Sigma-Aldrich, 98%), urea (Fluka, 99.5%) and deionised water with a molar ratio of 1/0.27/300. The mixture has been kept for 12 h at 110 °C in an autoclave [15]. The R2 catalyst has been obtained by dissolving cobalt acetate (Sigma-Aldrich, 98%) 0.45 M with the desired amount of polyethyleneglycol (PEG 10,000, Merck) as surfactant (9/0.1 molar ratio). Then the resulting homogeneous solution has been precipitated adding dropwise an urea solution 0.9 M until a molar ratio cobalt acetate/urea of 1/2 is attained. The mixture has been then transferred to an autoclave and subsequently heated at 100 °C for 6 h [16].

2.2.2. Samples with sheet-like morphology (S samples – 2D shaped catalysts)

The S1 sample has been prepared by dissolving cobalt(II) nitrate (Sigma-Aldrich, 98%) and polyvinylpyrrolidone (PVP40, Sigma-Aldrich) (1/0.01 molar ratio) in a mixture of 50% v/v of formaldehyde (Sigma-Aldrich, 37%) and deionised water, with a $\text{Co}/\text{H}_2\text{O}$ molar ratio of 1/65. Then, 0.4 M NaOH (Panreac, 99%) (Co/NaOH 1/0.2) has been slowly added to the solution. Finally, the mixture has been heated at 120 °C for 12 h [17]. For synthesising the S2 sample, cobalt(II) nitrate (Sigma-Aldrich, 98%) has been dissolved in deionised water (with a molar ratio of 1/1000). Triethylamine (TEA, Panreac, 99.5%) has been added to attain a Co/TEA of 1/0.366 molar ratio. The mixture has been maintained at 140 °C for 12 h [18].

2.2.3. Samples with cube-like morphology (C samples – 3D shaped catalysts)

The C1 sample has been synthesised from a mixture of cobalt (II) acetate tetrahydrate (Sigma-Aldrich, 98%), PVP and deionised water with a molar ratio of 1/0.02/445. Once the mixture is heated at 90 °C an ammonia solution (Panreac, 25%) is added dropwise until the pH reaches 8.5. Finally, 1.35% of hydrogen peroxide solution (Sigma-Aldrich, 30%) has been added while maintaining a $\text{Co}/\text{H}_2\text{O}_2$ molar ratio of 1/0.05. The final solution has been kept at 90 °C for 5 h [19]. The C2 sample has been prepared from cobalt(II) acetate, using polyethyleneglycol (PEG 20,000, Merck) as template

(1/0.04 molar ratio) and a mixture of 50% v/v of formaldehyde and deionised water, with a $\text{Co}/\text{H}_2\text{O}$ molar ratio of 1/275. Then, the mixture has been precipitated by adding KOH (Panreac, 85%) until the pH reaches 8.5. Finally, a hydrogen peroxide solution (Sigma-Aldrich, 30%) has been added with a $\text{Co}/\text{H}_2\text{O}_2$ molar ratio of 1/8. The final solution is kept at 90 °C for 5 h [20].

All the mixtures have been cooled down to room temperature after the hydrothermal treatment. The resulting precipitates have been filtered and washed with deionised water. The samples have been then dried in an oven at 110 °C overnight followed by a calcination step in static air with a heating ramp of 10 °C min⁻¹ and held for 4 h at 500 °C. Next, catalyst pellets with a 0.3–0.5 mm diameter have been prepared by a process of compressing the oxide powders into flakes in a hydraulic press (Specac), crushing and sieving.

2.2. Characterisation techniques

Textural properties have been evaluated from the nitrogen adsorption–desorption isotherms, determined at –196 °C with a Micromeritics TRISTAR II apparatus. The specific areas of the samples were determined in line with standard BET procedure. Mean pore size was calculated using the BJH method. The samples have been previously degassed overnight with N₂ flow.

X-ray diffraction (XRD) studies have been carried out on a X'PERT-MPD X-ray diffractometer with Cu K α radiation ($\lambda = 1.5406 \text{ \AA}$) and Ni filter. The X-ray tube is operated at 30 kV and 20 mA. Samples have been scanned from 5° < 2θ < 80° and the X-ray diffraction line positions have been determined with a step size of 0.02° and counting time of 2.5 s per step. Phase identification has been conducted by comparison with JCPDS (Joint Committee on Powder Diffraction Standards) database cards. The structural analysis the Co and Si species were evaluated with their electronic transitions by diffuse reflectance UV-vis and near infrared spectroscopy (DR-UV-vis-NIR) with a Jasco V-570 apparatus in the 2300–200 nm wavenumber range.

Raman spectra, acquired using a Leica 50 x N Plan (0.75 aperture) lens, have been recorded with a Renishaw InVia Raman spectrometer coupled to a Leica DMLM microscope. The spectrometer is equipped with a 514-nm laser (ion-argon laser, Modu-Laser) with a nominal power at the source of 50 mW and a maximum power at the sample of 20 mW. Ten seconds are employed for each spectrum, and 20 scans are accumulated with 10% of the maximum power in the spectral window from 150 to 1200 cm⁻¹.

X-ray photoelectron spectroscopy studies have been performed using in a SPECS system with equipped with Phoibos 150 1D analyzer and DLD-monochromatic radiation source. Scanning electron microscopy (SEM) images have been studied using Schottky (JEOL JSM-7000F) equipment with a resolution of 30 kV. Drops of emulsions, created by sonication of the powder samples in ethanol, were deposited on C coated Cu grids and left in air to dry.

HRTEM measurements were carried out at FEI Titan Cubed G2 60-300 electron microscope at 300 kV equipped with a high-brightness X-FEG Schottky field emission electron gun and a monochromator and CEOS GmbH spherical aberration (Cs) corrector on the image side. The images were recorded on a charge-coupled device (CCD) camera (2kx2k Gatan UltraScanTM 1000). The samples were prepared by dispersion into ethanol solvent and keeping the suspension in an ultrasonic bath for 15 min, after a drop of suspension was spread onto a TEM copper grid (300 mesh) covered by a holey carbon film followed by drying under vacuum.

Redox behaviour has been examined by temperature-programmed reduction experiments (TPR). These experiments have been conducted on a Micromeritics Autochem 2920 instrument. Firstly, all the samples (20 mg) have been pre-treated in an oxygen stream (5% O₂/He) at 400 °C for 1 h, and then cooled down

to room temperature. The reducing gas used in all experiments is 5%H₂ in Ar, with a flow rate of 50 cm³ min⁻¹. The temperature range explored is from room temperature to 500 °C with a heating rate of 10 °C min⁻¹. This temperature has been maintained for 0.5 h. The water produced by the reduction process is trapped into a cold trap. The gas stream at the exit is also on-line analysed by mass spectrometry (MS) in order to verify the absence of water. The consumption of H₂ has been quantitatively measured by time integration of TPR profiles. During this test, the reduction of Co₃O₄ to Co is assumed to be complete since no hydrogen consumption has been registered when a second TPR run is performed.

Oxygen storage complete capacity (OSCC) measurements have been taken using a Micromeritics ASAP 2020 equipment. The samples have been outgassed at 150 °C for 16 h to clean the surface. Afterwards the temperature has been increased up to 325 °C. Next the samples have been subjected to a reduction treatment with a pure hydrogen stream at constant temperature (325 °C) for 30 min. The sample has been then purged with helium, and the measurement of oxygen consumption at constant temperature has been taken.

2.3. Catalyst activity determination

Catalytic tests have been performed in a bench-scale fixed bed reactor (Microactivity modular laboratory system provided by PID Eng&Tech S.L.) operated at atmospheric pressure and fully monitored by computer. The reactor is made of quartz with an internal diameter of 10 mm and a height of 300 mm, in which the temperature is controlled with a thermocouple placed in the catalyst bed. Typically 0.85 g of catalyst in powdered form (0.3–0.5 mm) is loaded. The reaction feed consists of 1000 ppm of DCE in dry air with a total gas flow of 500 cm³ min⁻¹. The corresponding gas hourly space velocity is 30,000 h⁻¹. The amount and particle size of catalyst and the total gas flow rate are chosen in order to be out of the internal and external diffusion limits. Catalytic activity has been measured over the range 150–500 °C and conversion data have been calculated by the difference between inlet and outlet concentrations. Conversion measurements and product profiles are taken at steady state, typically after 30 min on stream. Either product selectivity is calculated based on either chlorine or carbon atoms present in that product divided by the total chlorine or carbon atoms present in the product stream (expressed as%). The feed and effluent streams have been analysed using an on-line 7980A Agilent Technologies gas chromatograph equipped with a thermal conductivity detector (CO and CO₂) and an electron capture detector (chlorinated hydrocarbons). Analysis of HCl and Cl₂ has been carried out by means of ion selective electrode and titration, respectively. Further details on analytical procedures are described elsewhere [21].

3. Results

3.1. Physicochemical characterisation of Co₃O₄ samples

The textural properties in terms of BET surface area and pore volume are shown in Table 1. The surface area is between 16 and 19 m² g⁻¹, except for the R1 sample, which exhibits a remarkably lower value (6 m² g⁻¹), and the C1 sample (33 m² g⁻¹), which, in contrast, shows by far the largest surface area. The pore volume follows a consistent trend with respect to the surface area. Hence the largest pore volume (0.21 cm³ g⁻¹) is found for the C1 sample.

The structural properties are characterised by XRD using the JCPDS files as a reference. Fig. 1 shows the XRD patterns of the six samples calcined at 500 °C. For every catalyst all the reflection peaks, located at 20 19°, 31.3°, 36.8°, 44.8°, 59.3°, and 65.2°,

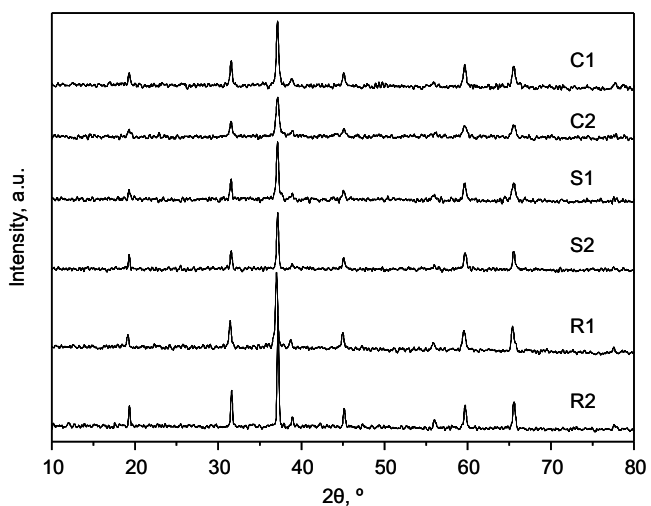


Fig. 1. XRD patterns of the synthesised Co₃O₄ samples.

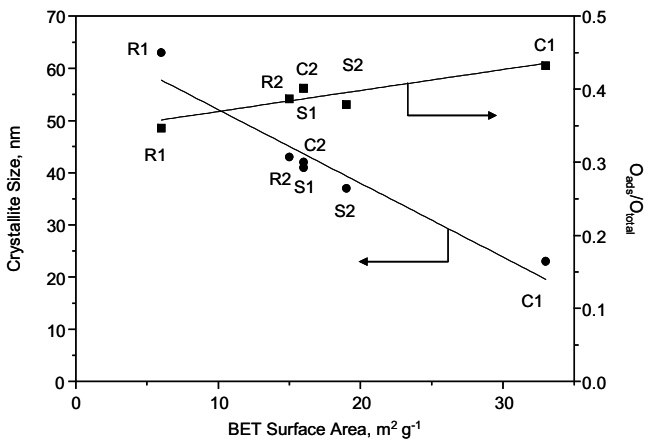


Fig. 2. Relationship among the BET surface area, crystallite size and O_{ads}/O_{latt} ratio for the synthesised Co₃O₄ samples.

can be assigned to a pure cubic phase of cobalt (II,III) oxide spinel (JCPDS 42-1467), irrespectively of the followed synthesis route. No diffraction peaks related to a CoO phase are detected. The average crystallite size, estimated from the full width half maximum of the characteristic diffraction peaks by applying the Scherrer equation (Table 1), is between 23 and 62 nm. Hence, on the basis of these values the set of samples can be classified into three groups: C1 (23 nm), C2, S1, S2 and R2 (with a relatively similar size in the 37–43 nm range) and R1 (63 nm). It is noticed that a clear inverse relationship between the surface area and the crystallite size exists, since the crystallite size decreases with the available surface area (Fig. 2). On the other hand, DR-UV-vis spectra of the samples (figure not shown) present two broad bands at 370–390 and 625–680 nm, and these are related to the spinel Co₃O₄ structure with the Co ions in tetrahedral and octahedral coordination, respectively [22].

In addition to giving a supplementary evidence for the formation of Co₃O₄ in all the samples, Raman spectroscopy is helpful in providing insights into the lattice distortion of the spinel catalysts. Hence, the spectra include five Raman bands (A_{1g} + E_g + 3F_{2g}) visible in the 100–800 cm⁻¹ range, at 198, 484, 522, 622 and 694 cm⁻¹ (Fig. 3) [23]. No additional bands corresponding to other phases, such as CoO, have been found in line with XRD results. However, a significant shift of the Raman bands towards lower frequencies, along with a slight increase in the full width at half-maximum of the peaks, is detected. These observations are associated with the for-

Table 1

Textural properties, crystallite size and surface composition of the synthesised Co_3O_4 samples.

Catalyst	Surface area, $\text{m}^2 \text{g}^{-1}$	Pore volume, $\text{cm}^3 \text{g}^{-1}$	Crystallite size, nm	$\text{O}_{\text{ads}}/\text{O}_{\text{latt}}$ (XPS)	$\text{Co}^{2+}/\text{Co}^{3+}$ (XPS)	$T_{50}, ^\circ\text{C}$	$T_{90}, ^\circ\text{C}$
R1	6	0.056	63	0.53	0.51	340	420
R2	15	0.160	43	0.63	0.69	310	390
S1	16	0.157	42	0.67	0.79	305	360
S2	19	0.182	37	0.61	0.61	315	360
C1	33	0.210	23	0.76	0.89	290	340
C2	16	0.156	41	0.67	0.76	305	370

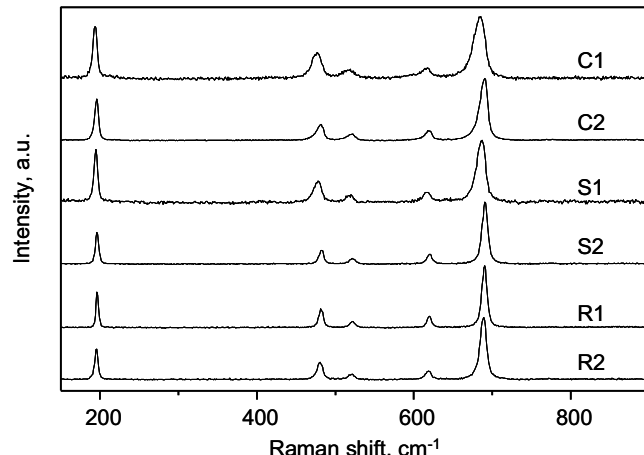


Fig. 3. Raman spectra of the synthesised Co_3O_4 samples.

mation of a highly defective structure [24]. The extent of the lattice distortion is thus larger for C1, S1 and C2 samples in comparison with S2, R1 and R2 samples.

Fig. 4 includes the SEM images of the six samples before and after the calcination step at 500°C . Before calcination the R1 sample (Fig. 4(a)) presents the desired rod-like morphology while this is not successfully attained in the case of the R2 sample (Fig. 4(c)). Unfortunately, the rod-like structure seems not to be stable with temperature since it transforms into irregular particles without any defined shape (Fig. 4(b) and (d)). As for S samples, cobalt crystals grow mainly in two directions (Fig. 4(e) and (g)). After calcination this morphology is essentially preserved although the vertexes are not so well defined and the sheets look more irregular (Fig. 4(f) and (h)) with respect to their counterparts before calcination. Particularly, in the case of the calcined S2 sample some holes appear on the surface of the nanosheets which are supposed to be formed during the calcination of the organic surfactant. Also a substantial number of nanoparticles along with the nanosheets are visible. Finally the micrographs of the cube-like samples (C samples) before (Fig. 4(i) and (k)) and after calcination (Fig. 4(j) and (l)) are shown. For the C1 sample the 3D structure is homogeneous and thermally stable. Nevertheless, although the cube structure is massively attained for the C2 sample, largest sheets are clearly formed as well after calcination. Moreover, some cube-shaped crystals loose their regular morphology due to a strong sinterisation. It can be therefore concluded that after calcination of the various cobalt precursors only the desired thermally stable, homogeneous morphology (nanocubes) is achieved in the case of C1 sample. As for C2, S1 and S2 samples a mixture of cubes and sheets (C2 sample) and a mixture of sheets and irregular discrete particles are obtained (S1 and S2 samples). On the other hand, both R1 and R2 samples should be considered catalysts with a poor morphological stability characterised by an ill-defined (amorphous) structure upon calcination, similar to that obtained when using a simple synthesis route such as calcination of a cobalt precursor salt [25].

Fig. 5 shows some representative HRTEM images of selected nanosheets (S1 sample) and nanocubes (C1 sample). From the lattice resolved image of the S1 sample and its corresponding Fast Fourier Transform (FFT) spot pattern, two lattice spaces of 0.28 nm and 0.47 nm are observed, which correspond to the {220} and {111} planes of Co_3O_4 , thereby indicating that {112} was the dominant exposed facets of the nanosheet sample. By contrast, the dominant exposed planes of the C1 sample are {001}, which are the only planes normal to the set of {220} planes with a lattice space of 0.28 nm.

XPS analysis has been employed to gain further insight into the composition and chemical state on the surface of the prepared bulk oxides. As shown in Fig. 6, a broad peak is identified in the O 1s spectra of all samples, thereby indicating the existence of several types of surface oxygen species with varying chemical states. Hence, this asymmetrical band has been decomposed into two components at 529.8 and 530.9 eV. The former is attributed to surface lattice oxygen (O_{latt}) species, whereas the latter corresponds to surface adsorbed oxygen (O_{ads}) species [26,27]. Data listed in Table 1 reveal that the $\text{O}_{\text{ads}}/\text{O}_{\text{latt}}$ molar ratio is significantly higher in the case of the C1 sample (0.76). In contrast the sample R1 exhibits the lowest value (0.53). As for C2, S1, S2 and R2 samples the ratio is relatively similar, in the 0.61–0.67 range, which is in agreement with their comparable surface area and crystallite size (Fig. 1). In sum, this difference in $\text{O}_{\text{ads}}/\text{O}_{\text{latt}}$ molar ratios suggests that the selected synthesis route has an important influence on the relative amount of surface oxygen vacancies.

On the other hand, Co 2p spectra display two intense bands at 780.7 and 796.1 eV, which are related to the $\text{Co} 2p^{3/2}$ and $\text{Co} 2p^{1/2}$ spin-orbital peaks of Co_3O_4 spinel. The energy difference between these two features is found to be around 15.4 eV. This value fairly agrees with those reported in the literature, and suggested that the existence of Co(II) and Co(III) on the surface of the samples [28–30]. Since the analysis of $2p^{1/2}$ and $2p^{3/2}$ components provides the same chemical information, only the $2p^{3/2}$ spectra have been deconvoluted with a non-linear least squares fitting programme using Gaussian component curves after background subtraction according to Shirley (Fig. 7). The features have been thus fitted into two peaks located at 794.6 and 797.1 eV corresponding to Co^{3+} and Co^{2+} , respectively. It must be pointed out that a certain amount of CoO was observed on the surface of all the cobalt catalysts, as revealed by the XPS signal at 783 eV [29]. The contribution of this species was estimated to be roughly similar on the samples and lower than 10% of the total amount of cobalt. Table 1 lists the $\text{Co}^{2+}/\text{Co}^{3+}$ ratios deduced from the relative areas of each band. Since the population of adsorbed oxygen species on the surface of the spinels is governed by a higher concentration of Co^{2+} [9], that is, by a larger difference in the $\text{Co}^{2+}/\text{Co}^{3+}$ molar ratio with respect to the theoretical value (0.5), a high value of this parameter can be taken as an indication of a higher amount of oxygen defects, which are compensated by adsorbed oxygen species close to the surface. As shown in Fig. 8, a good agreement between $\text{Co}^{2+}/\text{Co}^{3+}$ and $\text{O}_{\text{ads}}/\text{O}_{\text{lattice}}$ exists. Judging from these results the C1 sample with a cube-shaped morphology is the spinel with a higher surface concentration of Co^{2+} and oxygen adspecies, while the R1 sample presents the opposite behaviour.

The amount of oxygen defects is closely connected with a favoured oxygen mobility within the lattice. In other words, a good relationship should exist between the O_{ads}/O_{latt} ratio and the low-temperature reducibility of the samples. This latter property has been characterised by H₂-TPR (Fig. 9). The reduction profiles essentially present two peaks corresponding to a two-step reduction process [9,24]. In the case of the R1 sample the definition of these two bands is less evident, probably due its largest particle size and smallest surface area [18]. The first feature is associated with the reduction of Co⁺³ ions to Co⁺² that involves the formation of CoO, while the second peak is attributed to the subsequent reduction of CoO to metallic cobalt. Ideally the H₂ uptake of these two steps is 1:3. A quantitative evaluation of the amounts of hydrogen consumed during reduction (about 16.6 mmol H₂ g⁻¹) reveal that in all cases Co₃O₄ is reduced completely into metallic cobalt at 400 °C.

Taking as a criterion the temperature at which a degree of reduction of 5% is attained, the onset of the reduction of the C samples occurs at the lowest temperatures (about 170 °C for the

C1 sample and 190 °C for the C2 sample). On the other hand, the reduction of the S samples and the R2 sample starts at about 200 °C while the R1 sample requires notably higher temperatures, close to 235 °C. The good reducibility of the nanocube-shaped samples is also confirmed by its low-temperature reduction peak about 270 °C. By contrast, the S samples and R2 sample are characterised by a slightly higher peak temperature (280–285 °C) while the R1 sample requires substantially higher temperatures (310 °C). All these findings (Table 2) clearly suggest that the reducibility is particularly enhanced for the C1 sample due its larger amount of highly reactive oxygen species as also evidenced by XPS analysis.

Another key property for controlling the catalytic activity of cobalt oxide samples is their ability to recover their original oxidised phase in the presence of gaseous oxygen. Thus, the oxygen storage complete capacity is proposed as a meaningful analysis as it represents the total amount of O₂ consumed after reduction at constant temperature. This sequential titration with H₂ and O₂ is therefore helpful in indentifying the amount of trivalent cobalt

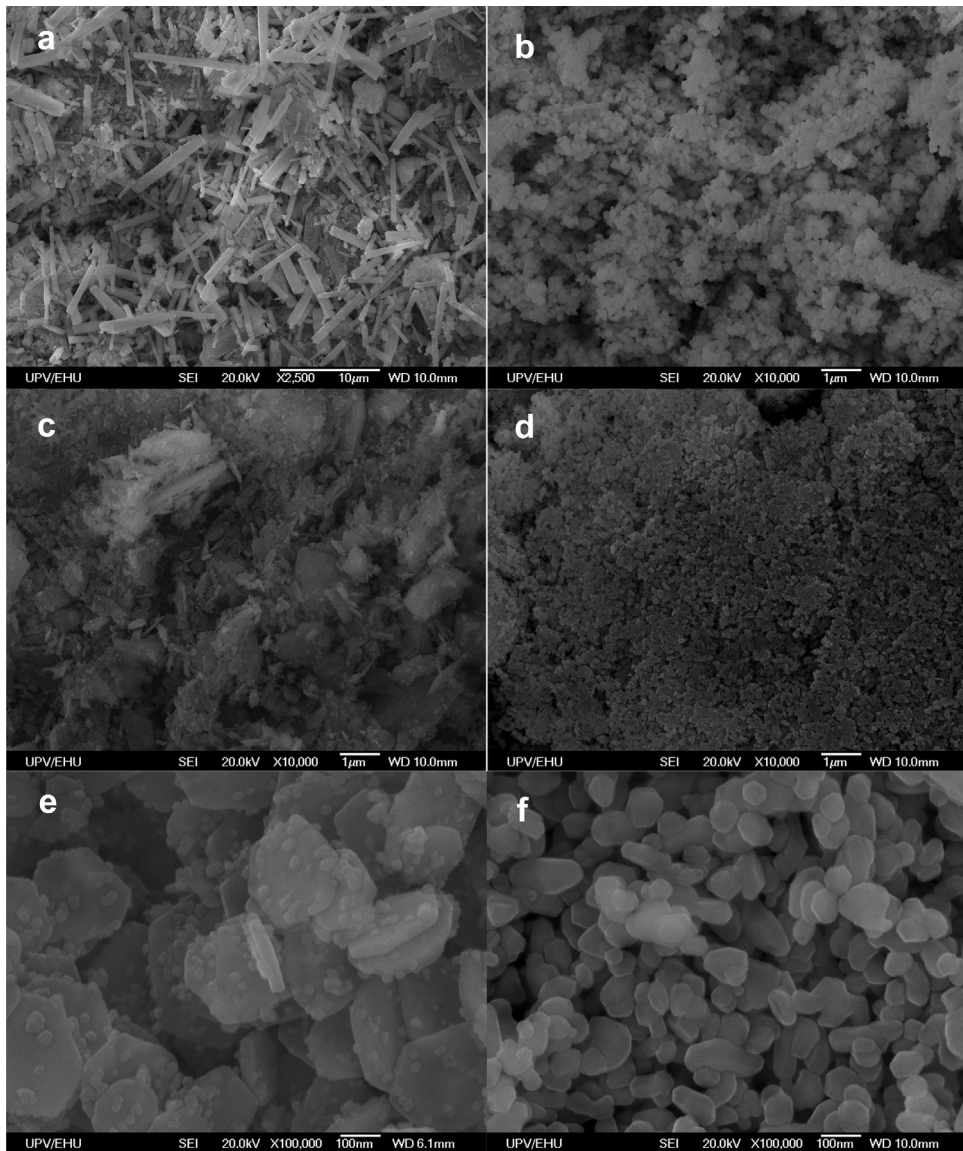


Fig. 4. SEM images of the synthesised Co₃O₄ samples before (a,c,e,g,i,k) and after calcination at 500 °C (b,d,f,h,j,l). R1 sample (a,b); R2 sample (c,d); S1 sample (e,f); S2 sample (g,h); C1 sample (i,j); C2 sample (k,l).

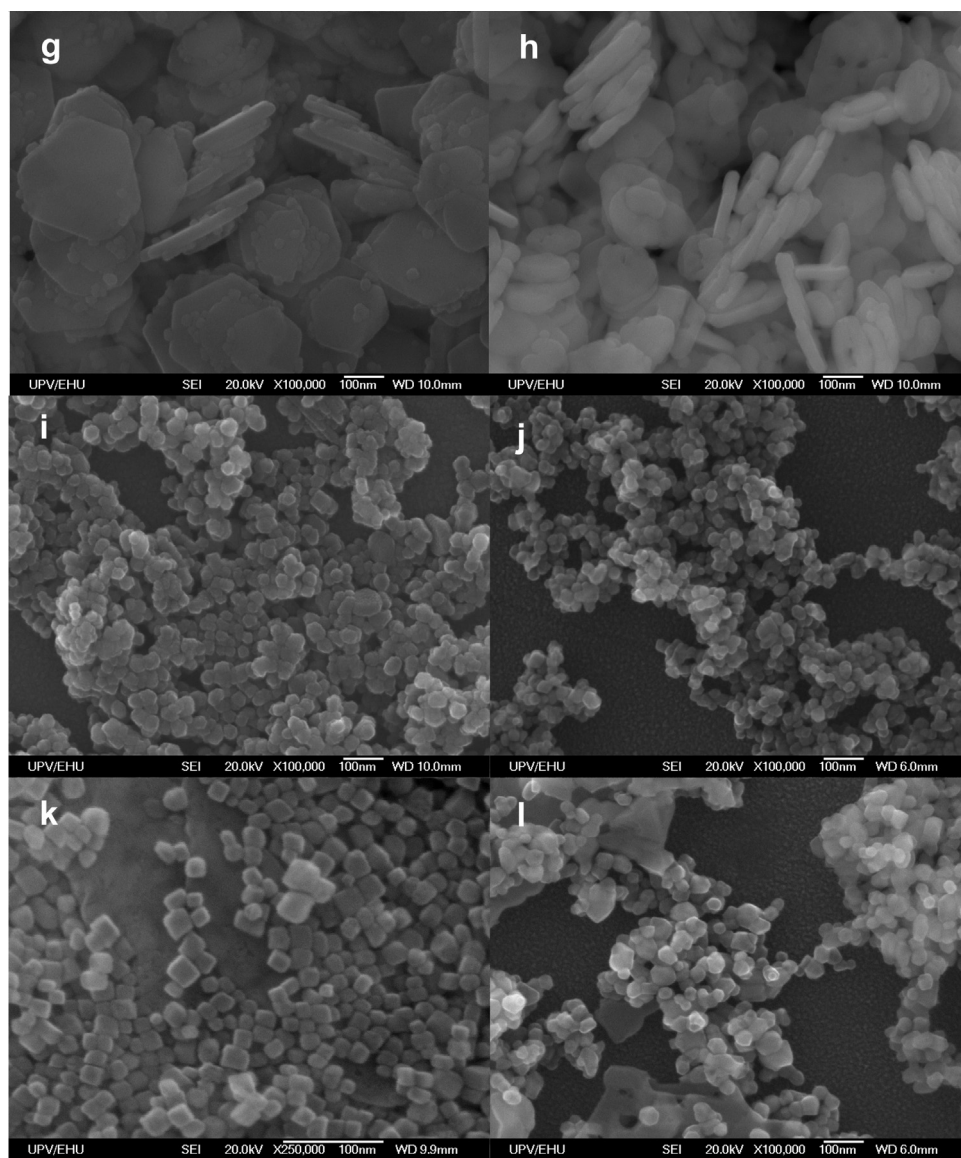


Fig. 4. (Continued).

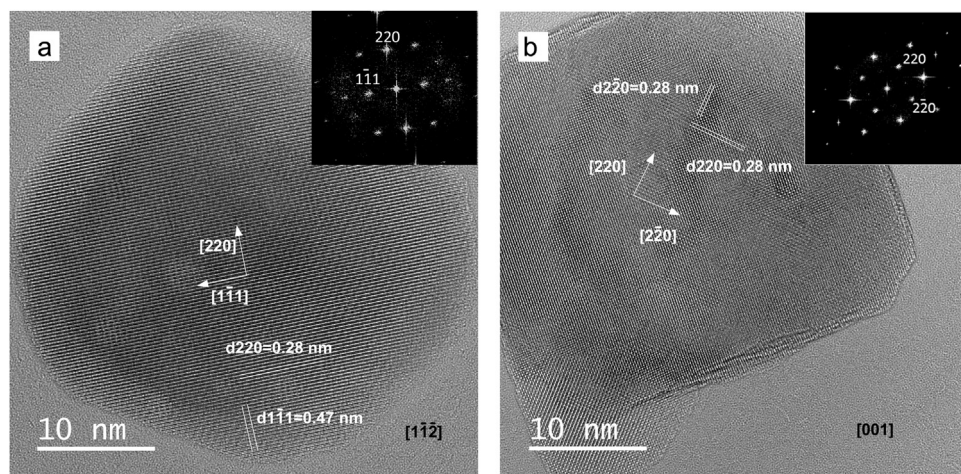


Fig. 5. HRTEM images and Fast Fourier Transform spot patterns of the nanosheet S1 sample (a) and the nanocube C1 sample (b).

Table 2

Results from H₂-TPR and OSCC of the synthesised Co₃O₄ samples and T₅₀ and T₉₀ values for DCE oxidation.

Catalyst	Onset reduction temperature ^a , °C	Low-temperature reduction peak, °C	Degree of reduction (325 °C), %	Oxygen storage complete capacity (325 °C), mmol O ₂ g ⁻¹	T ₅₀ , °C	T ₉₀ , °C
R1	235	310	28	7.2	340	420
R2	200	285	53	7.5	310	390
S1	200	280	57	8.1	305	360
S2	205	285	47	7.6	315	360
C1	170	270	61	8.4	290	340
C2	190	280	56	8.1	305	370

^a Temperature at which a degree of reduction of 5% is achieved.

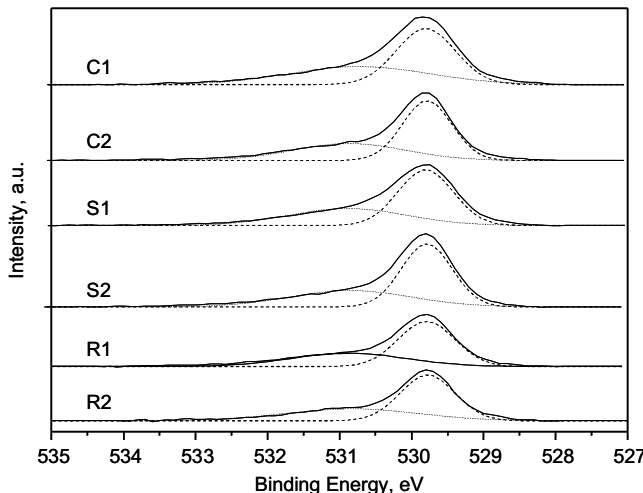


Fig. 6. O 1s XPS spectra of the synthesised Co₃O₄ samples.

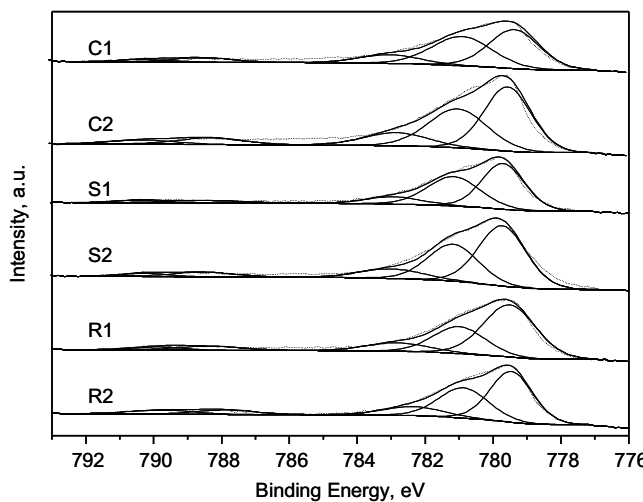


Fig. 7. Co 2p^{3/2} XPS spectra of the synthesised Co₃O₄ samples.

species that are workable under reaction. A fixed temperature of 325 °C is selected since it provides, as will be shown later on, a significant DCE conversion in the 40–85% range for all the cobalt catalysts. The results are included in Table 1. The highest O₂ uptake (8.1 mmol O₂ g⁻¹) is found for the C1 sample while it is in the 7.1–7.4 mmol O₂ g⁻¹ range for the rest of the samples except for the R1 sample that shows the lowest consumption (6.8 mmol O₂ g⁻¹). In sum, results from both H₂-TPR and OSCC revealed a better redox behaviour for the C1 sample. This property seems to be closely related to the high surface area, low crystallite size and high population of oxygen defects exhibited by the nanocube-shaped C1 sample. Fig. 8 shows that the existence of a higher amount of oxygen

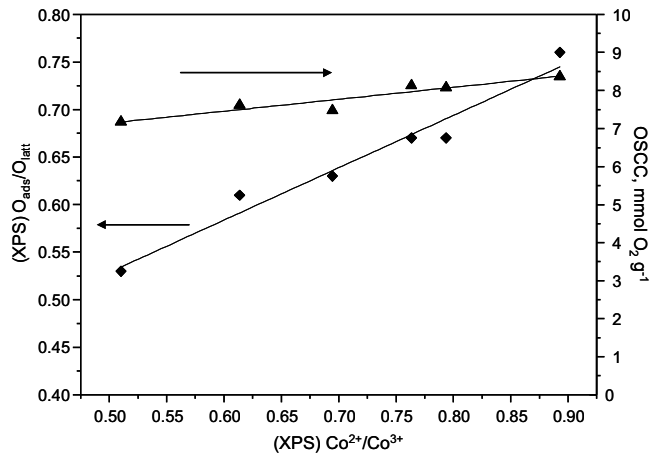


Fig. 8. Relationship among surface Co²⁺/Co³⁺ ratio, surface O_{ads}/O_{latt} ratio and oxygen storage complete capacity (325 °C) for the synthesised Co₃O₄ samples.

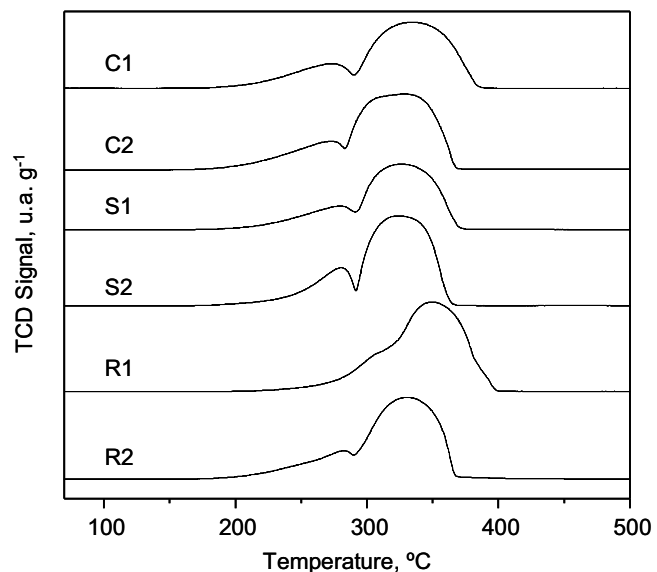


Fig. 9. H₂-TPR profiles of the synthesised Co₃O₄ samples.

defects (evidenced by a high surface Co²⁺/Co³⁺ ratio) enhances the oxygen mobility in the lattice as revealed by the promoted reduction at low temperatures and the larger oxygen storage capacity after partial reduction.

3.2. Catalytic activity of the Co₃O₄ samples

1,2-Dichloroethane was taken as a model for the category of double carbon chlorinated VOCs with a H/Cl ratio of >1. When compared with double carbon olefins such as dichloroethylene and

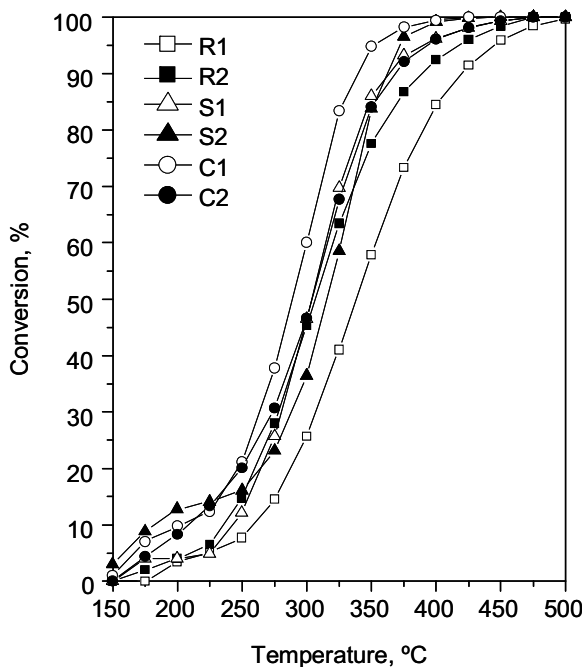


Fig. 10. Light-off curves of DCE oxidation over the synthesised Co_3O_4 samples.

trichloroethylene, DCE typically requires lower destruction temperatures [31]. The light-off curves are plotted in Fig. 10, whilst the T_{50} and T_{90} values (temperature needed to attain 50 and 90% conversion, respectively) are listed in Table 1. It must be pointed out that DCE conversion in the absence of any catalyst does not occur below 350 °C and reaches only 20% conversion at 500 °C. In contrast, the use of Co_3O_4 as catalyst significantly accelerates the desired reaction, and in all cases the chlorinated compound is completely (>95% conversion) abated above 450 °C.

Nevertheless, substantial differences are clearly evident depending on the nanostructure of the sample, thus revealing that the preparation method is a key factor for obtaining a highly active Co_3O_4 catalyst. Hence, the temperature range at which the 50% conversion is achieved varies between 290 and 340 °C, whereas the temperature for complete removal (90% conversion) is in the 340–420 °C range. On the basis of T_{50} values the catalytic activity follows this trend: C1 > C2 ≈ S1 > S2 ≈ R2 > R1. Therefore, it can be established that nanocubes are more efficient than samples with a mixed morphology consisting of nanosheets and nanoparticles (S samples) and nanoparticles without a well-defined nanostructure (R samples).

Hu et al. [13] reported a high activity in methane oxidation of Co_3O_4 catalysts with sheet-like nanostructure in comparison with samples with a cube-like morphology. For these samples calcined at 350 °C the observed catalytic activity was consistent with a better redox behaviour, which in turn, was assigned to the more reactive surface of the {112} planes. In this work at temperatures below 225 °C (with a conversion lower than 15%) the S2 sample exhibits a remarkable behaviour followed by the C samples, which in principle could be taken as an evidence of the higher intrinsic activity of the surface of {112} planes with respect to that of surfaces of {001}. However this active performance is not maintained with increased temperature. Between 250–400 °C the best behaviour is clearly displayed by the C1 sample with a nanocube-shaped morphology. This observation could be related to the markedly higher calcination temperatures (500 °C) used in our study. As revealed by SEM this severe thermal treatment provokes significant morphological defects in the nanosheets. The nanostructure of C samples is, however, more stable with temperature. Hence, it can be con-

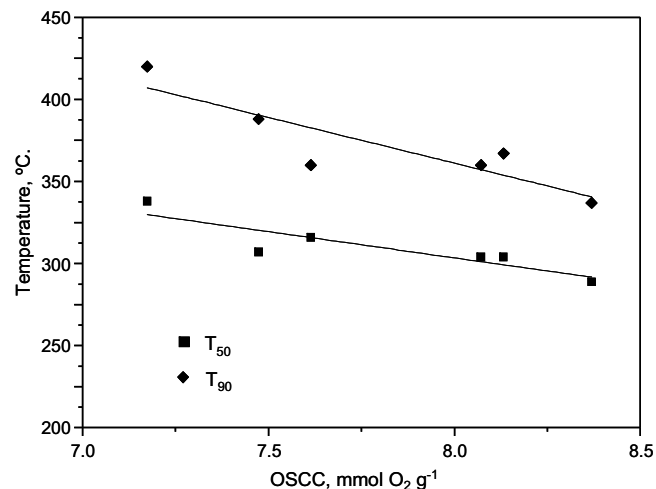


Fig. 11. Dependence of T_{50} and T_{90} values with the oxygen storage complete capacity (325 °C) for the synthesised Co_3O_4 samples.

cluded that the cube-like nanostructure provides exposed facets that better preserved their surface activity after calcination at high temperature.

Based on the characterisation results and catalytic data it is postulated that the oxidation of DCE is controlled by oxygen mobility in the lattice and subsequent fast re-oxidation of the reduced metal oxide by oxygen present in the gas phase. In other words the mass catalytic activity is higher for samples exhibiting a facile participation of oxygen species and a good ability to recover its initial oxidised phase (Fig. 11). It is widely reported that this favoured mobility is catalytically relevant when using Co_3O_4 catalysts for the oxidation of relatively recalcitrant hydrocarbons such as oxylene [32], 1,2-dichlorobenzene [33], toluene [34] and methane [35]. Note that in view of the observed temperature range required for oxidation of DCE (>300 °C), this VOC could fall into the category of stable hydrocarbons (where methane is the main representative compound).

Ultimately the generation of active oxygen species is dependant on the surface area and the crystallite size of the spinel. It seems clear that these properties are optimised for the cube-shaped catalysts (particularly, for the C1 sample). For the oxidation of DCE, which requires relatively high temperatures and consequently a previous proper thermal activation to avoid structural changes during reaction, the 3D morphology is thermally more stable than 2D one. In this regard no clear conclusions can be extracted from the suitability of nanorods since the synthesis routes employed in this work have failed to attain this desired morphology.

3.3. Kinetic analysis

Activity data have been kinetically analysed considering pseudo-first kinetics in DCE and zero order for oxygen. This power-law dependence is coherent with a simplified Mars van Krevelen reaction rate equation under excess of O_2 conditions. It was previously checked that operating with a linear velocity higher than 7 cm s^{-1} and catalyst particle sizes lower than 1 mm ensured that experimental data are not influenced by both external and internal mass-transfer resistances. The following linearised equation has been used to estimate the kinetic parameters for the integral fixed-bed reactor,

$$\ln[-\ln(1-X)] = \ln[(k_0 P_{\text{DCE}_0} (W/F_{\text{DCE}_0})] - E_a/RT \quad (1)$$

where X is the fractional conversion of DCE, k_0 is the pre-exponential factor of the Arrhenius equation, E_a is the apparent

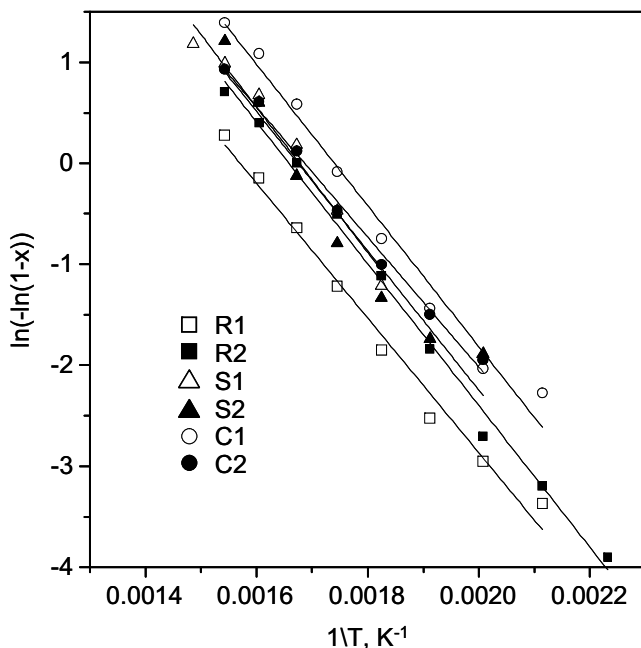


Fig. 12. Pseudo-first order fit for the experimental data obtained over the synthesised Co_3O_4 samples.

Table 3

Pseudo-first kinetic parameters for the oxidation of DCE over the synthesised Co_3O_4 samples.

Catalyst	$E_a, \text{kJ mol}^{-1}$	$\ln[k_0(W/F_{AO})P_{AO}]$	$k_0, \text{mol/s g}^{-1} \text{MPa}^{-1}$ ($\times 10^{-2}$)	r^2
R1	55.5 ± 2.7	10.5 ± 0.6	1.4	0.99
R2	58.4 ± 1.6	11.6 ± 0.4	4.5	0.99
S1	59.8 ± 4.8	12.1 ± 0.9	6.8	0.97
S2	59.9 ± 4.2	12.1 ± 0.9	7.3	0.97
C1	58.1 ± 3.2	12.2 ± 0.7	7.6	0.98
C2	53.5 ± 1.9	10.9 ± 0.4	2.1	0.99

activation energy, W is the catalyst mass and F_{DCEO} is the inlet DCE molar flow. The activation energies derived from the plots in Fig. 12 are relatively similar ($53\text{--}60 \text{ kJ mol}^{-1}$) within the experimental error for all the samples, and close to the reported values in the literature for the oxidation of chlorinated alkanes over transition metal oxides [36–38]. This suggested that the reaction mechanism is essentially the same irrespective of the examined Co_3O_4 catalyst. The values of the pre-exponential factor and the apparent activation energy for the six cobalt oxide samples, as well as the regression coefficients, are included in Table 3. Fig. 13 shows the relationship between the experimental conversion values and the conversion values dictated by the kinetic model (solid line). The results presented in this figure demonstrate that the proposed kinetic rate expression provides a reasonably accurate data correlation over the wide range of temperatures investigated ($150\text{--}500^\circ\text{C}$). Only the data obtained from the S2 sample shows a significant deviation consistently with the poorer fit of the experimental data.

3.4. Product distribution and stability

In addition of a high conversion at the lowest temperatures the goodness/suitability of a catalyst for chlorinated VOC removal is also influenced by a limited or ideally negligible ability to yield by-products coming from an incomplete conversion of the feed. In other words, the catalyst must show a complete selectivity to carbon dioxide in the temperature window at which conversion

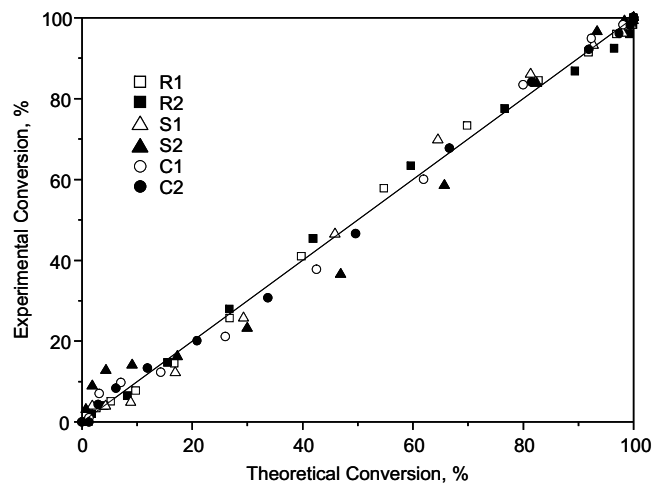


Fig. 13. Comparison of experimental data (symbols) and computed values (solid lines; power-law model) from conversions of the rate equation at different temperatures.

is higher at least than 95%. Hence, the product distribution of the most active cobalt catalyst (C1 sample) at 400°C (with a conversion close to 100%) has been analysed. Interestingly selectivity to CO_2 was complete and no traces of CO or chlorinated by-products were observed. These results are in stark contrast with those obtained with other metal oxides catalysts, such as Mn_2O_3 and CeO_2 . Hence, under identical reaction conditions at 400°C CO selectivity over CeO_2 is as high as 50% while CO_2 selectivity was about 70–90% over Mn_2O_3 [39,40]. When compared with supported noble metals such as $\text{Pd}/\text{Al}_2\text{O}_3$ or $\text{Pt}/\text{Al}_2\text{O}_3$, only platinum catalysts show a comparable excellent selectivity to CO_2 (100%) while significant amounts of CO are detected in the case of the palladium catalyst [41]. At lower reaction temperatures, although no CO was noticed, significant amounts of vinyl chloride, carbon tetrachloride, tetrachloroethylene, trichloroethylene or dichloroethylene were detected.

The absence of chlorinated by-products in the product stream of the C1 catalyst operated at 400°C is consistent with the only presence of HCl and Cl_2 as deep oxidation products. Although DCE has a H/Cl ratio larger than 1, which in principle should be enough to give HCl exclusively, the generation of large amounts of molecular chlorine is associated with the appreciable activity of Co_3O_4 at 400°C in the Deacon reaction ($2\text{HCl} + \frac{1}{2}\text{O}_2 \leftrightarrow \text{Cl}_2 + \text{H}_2\text{O}$). In fact, about 50% of the fed chlorine atoms are converted into Cl_2 . The relative abundance of HCl/ Cl_2 in the exit stream decreases with temperature (from 400 to 500°C) due to the increased rate of the Deacon reaction.

Finally, attention has been paid to examining the stability of the C1 sample when operating at constant temperature during a relatively prolonged time on stream (120 h). An operation temperature of 325°C (with a conversion well below 100%) has been selected which is suitable for observing eventual changes of the catalyst performance. Results shown in Fig. 14 revealed a relatively stable conversion (about 80%) and 100% selectivity to CO_2 . The used catalyst has been characterised by BET measurements, XRD and SEM-EDX. The BET surface area has decreased by 15%, whilst Co_3O_4 crystallite size remains virtually unaltered (24 nm vs 23 nm for the fresh sample). On the other hand, SEM analysis has revealed that the cube morphology is preserved. Moreover, no evidence of the formation of CoO , with an expected lower catalytic activity, is noted. Finally, EDX analysis indicates the presence of small amounts of chlorine on the sample, about 0.6%. Expectedly these minor changes do not seem to strongly influence the performance of the catalyst.

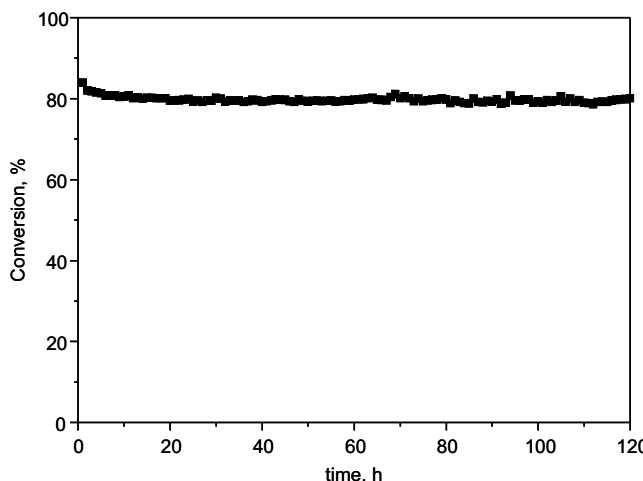


Fig. 14. DCE oxidation over the C1 sample at 325 °C as a function of time on stream.

4. Conclusions

The synthesis of bulk Co_3O_4 with different morphologies namely, nanorods, nanosheets and nanocubes, has been attempted with the aim to obtain highly active, selective and stable catalysts for the oxidation of 1,2-dichloroethane. Only in the case of cube-shaped samples (C samples) the desired nanostructure has been successfully achieved. Besides, these samples are thermally stable after calcination at 550 °C. As for the approaches devoted to the preparation of nanosheets (S samples), these indeed have led to this morphology although in mixture with discrete nanoparticles. Contrastingly, the methodologies used for the synthesis of nanorods (R samples) have not given satisfactory results as nanoparticles with an ill-defined structure were obtained.

The cube-shaped samples, particularly that prepared with polyvinylpyrrolidine as organic template, exhibit the highest surface area and the smallest crystallite size. In addition, this catalyst is characterised by a highly defective structure that involves a high concentration of oxygen vacancies at the surface in agreement with a favoured presence of Co^{2+} species. These all properties have a beneficial impact on reducibility at low temperatures and, in turn, on the catalytic activity for chlorinated VOC oxidation, thereby showing a morphology-dependent effect. These oxygen vacancies act as active sites since its replenishment is achieved by highly mobile oxygen species (O^{2-}) coming from the surface that ultimately oxidise the chlorinated hydrocarbons following a Mars van Krevelen mechanism. As a consequence, nanocubes show the best catalytic performance in the investigated oxidation reaction since they also exhibit a great ability to recover their original oxidised phase in the presence of gaseous oxygen.

Activity data reasonably correlate with a simplified Mars van Krevelen equation reaction rate in excess of oxygen. A comparable activation energy (53–60 kJ mol⁻¹) is deduced for all the synthesised samples. As for product distribution it must be pointed out that most of Co_3O_4 catalysts are highly selective to CO_2 . At 400 °C no oxidation by-products are detected only CO_2 , HCl and Cl_2 are produced. Finally it is worth noting that this optimised sample (with a nanocube morphology) is stable with time on stream (120 h) and no relevant physico-chemical changes are observed.

Acknowledgements

The authors wish to thank the financial support for this work provided by the Ministry of Economy and Competitiveness (ENE2013-41187-R), the Basque Government (Grant 2011/065,

IT657-13) and the University of The Basque Country (UFI 11/39). Technical and human support from SGiker (XRD (A. Larrañaga), XPS (B. Sánchez), Raman spectroscopy (A. Sarmiento) and HRTEM (M.L. No and A. Martínez)) is also gratefully acknowledged.

References

- [1] B. Huang, C. Lei, C. Wei, G. Zeng, Environ. Int. 71 (2014) 118–138.
- [2] S. Ojala, S. Pitkäaho, T. Laitinen, N.N. Koivikko, R. Brahmi, J. Gaállová, L. Matejová, A. Kucherov, S. Päivärinta, C. Hirschmann, T. Nevanperä, M. Riihimäki, M. Pirila, R.L. Keiski, Top. Catal. 54 (2011) 1224–1256.
- [3] H. Huang, Y. Xu, Q. Feng, D.Y.C. Leung, Catal. Sci. Technol. 5 (2015) 2649–2669.
- [4] L.F. Liotta, H. Wu, G. Pantaleo, A.M. Venezia, Catal. Sci. Technol. 3 (2013) 3085–3102.
- [5] T. Cai, H. Huang, W. Deng, Q. Dai, W. Liu, X. Wang, Appl. Catal. B 166 (2015) 393–405.
- [6] T. Garcia, S. Agouram, J.F. Sánchez-Royo, R. Murillo, A.M. Mastral, A. Aranda, I. Vázquez, A. Dejoz, B. Solsona, Appl. Catal. A 386 (2010) 16–27.
- [7] K. Zhou, J. Liu, P. Wen, Y. Hu, Z. Gui, Mater. Res. Bull. 67 (2015) 87–93.
- [8] B. Meng, Z. Zhao, X. Wang, J. Liang, J. Qiu, Appl. Catal. B 129 (2013) 491–500.
- [9] B. Solsona, T.E. Davies, T. García, I. Vázquez, A. Dejoz, S.H. Taylor, Appl. Catal. B 84 (2008) 176–184.
- [10] E. Escalera, M.A. Ballem, J.M. Córdoba, M.L. Antti, M. Odén, Powder Technol. 221 (2012) 359–364.
- [11] Y. Lv, Y. Li, W. Shen, Catal. Commun. 42 (2013) 116–120.
- [12] Z. Wang, W. Wang, L. Zhang, D. Jiang, Catal. Sci. Technol. (2016), <http://dx.doi.org/10.1039/C5CY01709B>.
- [13] L. Hu, Q. Peng, Y. Li, J. Am. Chem. Soc. 130 (2008) 16136–16137.
- [14] Z. Fei, S. He, L. Li, W. Ji, C.-T. Au, Chem. Commun. 48 (2012) 853–855.
- [15] Z. Wang, X. Chen, M. Zhang, Y. Qian, Solid State Sci. 7 (2005) 13–15.
- [16] G. Bai, H. Dai, J. Deng, Y. Liu, F. Wang, Z. Zhao, Appl. Catal. A 450 (2013) 42–49.
- [17] Y. Hou, H. Kondoh, M. Shimojo, T. Kogure, T. Otha, J. Phys. Chem. B 109 (2005) 19094–19098.
- [18] X. Liu, R. Yi, N. Zhang, R. Shi, X. Li, G. Qiu, Chem. Asian J. 3 (2008) 732–738.
- [19] Y. Li, J. Zhao, Y. Dan, D. Ma, Y. Zhao, S. Hou, H. Lin, Z. Wang, Chem. Eng. J. 166 (2011) 428–434.
- [20] Y. Yang, K. Huang, R. Liu, L. Wang, W. Zeng, P. Zhang, T. Nonferr, Metal Soc. 17 (2007) 1082–1086.
- [21] B. de Rivas, C. Sampedro, R. López-Fonseca, M.A. Gutiérrez-Ortiz, J.I. Gutiérrez-Ortiz, Appl. Catal. A-Gen. 417–418 (2012) 93–101.
- [22] L.F. Liotta, G. Pantaleo, A. Macaluso, G. Di Carlo, G. Deganello, Appl. Catal. A: Gen. 245 (2003) 167–177.
- [23] C.-B. Wang, Catal. Today 146 (2009) 76–81.
- [24] Q. Liu, L.C. Wang, M. Chen, Y. Cao, H.Y. He, K.N. Fan, J. Catal. 263 (2009) 104–113.
- [25] B. de Rivas, R. López-Fonseca, C. Jiménez-González, J.I. Gutiérrez-Ortiz, J. Catal. 281 (2011) 88–97.
- [26] C. Liu, Q. Liu, L. Bai, A. Dong, G. Liu, S. Wen, J. Mol. Catal. A-Chem. 370 (2013) 1–6.
- [27] Y. Du, Q. Meng, J. Wang, J. Yan, H. Fan, Y. Liu, H. Dai, Micropor. Mater. 162 (2012) 199–206.
- [28] B.M. Abu-Zied, S.M. Bawaked, S.A. Kosa, W. Schwieger, Appl. Surf. Sci. 351 (2015) 600–609.
- [29] S.A. Singh, G. Madras, Appl. Catal. A 504 (2014) 463–475.
- [30] S. Todorova, A. Naydenov, H. Kolev, K. Tenchev, G. Ivanov, G. Kadinov, J. Mater. Sci. 46 (2011) 7152–7159.
- [31] R. López-Fonseca, J.I. Gutiérrez-Ortiz, M.A. Gutiérrez-Ortiz, J.R. González-Velasco, J. Chem. Technol. Biotechnol. 78 (2003) 15–22.
- [32] Y. Wang, C. Zhang, Y. Yu, R. Yue, H. Hea, Catal. Today 242 (2015) 294–299.
- [33] T. Cai, H. Huang, W. Deng, Q. Dai, Wei Liu, X. Wang, Appl. Catal. B 166–167 (2015) 393–405.
- [34] S. Jiang, S. Song, Appl. Catal. B 140–141 (2013) 1–8.
- [35] A. Setiawan, E.M. Kennedy, B.Z. Dlugogorski, A.A. Adesina, M. Stockenhuber, Catal. Today 258 (2013) 276–283.
- [36] B. Chen, C. Bai, R. Cook, J. Wright, C. Wang, Catal. Today 30 (1996) 15–20.
- [37] S. Krishnamoorthy, J.P. Baker, M.D. Amiridis, Catal. Today 40 (1998) 39–46.
- [38] A. De Paoli, A. Barresi, Ind. Eng. Chem. 40 (2001) 1460–1464.
- [39] B. de Rivas, C. Sampedro, E.V. Ramos-Fernández, R. López-Fonseca, J. Gascón, M. Makkee, J.I. Gutiérrez-Ortiz, Appl. Catal. A 456 (2013) 96–104.
- [40] J.I. Gutiérrez-Ortiz, R. López-Fonseca, U. Aurrekoetxea, J.R. González-Velasco, J. Catal. 218 (2003) 148–154.
- [41] J.R. González-Velasco, A. Aranzabal, J.I. Gutiérrez-Ortiz, R. López-Fonseca, M.A. Gutiérrez-Ortiz, Appl. Catal. B 19 (1998) 189–197.